ASME Journal of Mechanisms and Robotics
Online journal at:
https://asmedigitalcollection.asme.org/mechanismsrobotics

Zhefeng Huang
Department of Biomedical Engineering,
Georgia Institute of Technology,
Atlanta, GA 30332
e-mail: zhuang480@gatech.edu

Hussain Alkhars
George Washington University School of Medicine,
Washington, DC 20052
e-mail: hma38@gwmail.gwu.edu

Anthony Gunderman
Department of Biomedical Engineering,
Georgia Institute of Technology,
Atlanta, GA 30332
e-mail: agunderman3@gatech.edu

Dimitri Sigounas
George Washington University School of Medicine,
Washington, DC 20052
e-mail: dsigounas@mfa.gwu.edu

Kevin Cleary
Sheikh Zayed Institute for Pediatric Surgical Innovation,
Children's National Health System,
Washington, DC 20010
e-mail: kcleary@childrensnational.org

Yue Chen[1]
Department of Biomedical Engineering,
Georgia Institute of Technology,
Atlanta, GA 30332
e-mail: yue.chen@bme.gatech.edu

Optimal Concentric Tube Robot Design for Safe Intracerebral Hemorrhage Removal

Purpose: The purpose of this paper is to investigate the optimal geometrical design of concentric tube robots (CTR) for intracerebral hemorrhage (ICH) evacuation, with a focus on minimizing the risk of damaging white matter tracts and cerebral arteries. Methods: To achieve our objective, we propose a parametrization method describing a general class of CTR geometric designs. We present mathematical models that describe the CTR design constraints and provide the calculation of a path risk value. We then use the genetic algorithm to determine the optimal tube geometry for targeting within the brain. Results: Our results show that a multi-tube CTR design can significantly reduce the risk of damaging critical brain structures compared to the conventional straight tube design. However, there is no significant relationship between the path risk value and the number and shape of the additional inner curved tubes. Conclusion: Considering the challenges of CTR hardware design, fabrication, and control, we conclude that the most feasible geometry for a CTR path in ICH treatment is a straight outer tube followed by a planar curved inner tube. These findings have important implications for the development of safe and effective CTRs for ICH evacuation by enabling dexterous manipulation to minimize damage to critical brain structures. [DOI: 10.1115/1.4063979]

Keywords: concentric tube robot design, intracerebral hemorrhage removal, path planning, medical robotics

1 Introduction

Intracerebral hemorrhage (ICH) is the most common subtype of hemorrhagic stroke with a 1-year mortality rate of 54% and 5-year mortality rate of 71% [1]. ICH is caused by bleeding from injured blood vessels that form a hematoma within the brain parenchyma. The expansion of this hematoma compresses the surrounding brain tissues, reducing oxygen delivery and inducing cellular damage, collectively known as a mass effect. It is hypothesized that evacuating a hematoma can reduce its mass effect [2], but studies have repeatedly shown that craniotomy and other conventional surgical interventions are not effective in treating this condition [3,4]. This is primarily due to the damage induced to healthy brain tissues along the path to deep-seated hematomas, offsetting any benefit surgery might provide [3].

To mitigate this damage and improve patient outcomes, clinicians have investigated minimally invasive approaches as an alternative to open surgery. These include stereotactic thrombolysis [5–12], endoscopic surgery [13–17], and stereotactic aspiration [18,19]. These treatment approaches have indicated promising results by minimizing disruption and scarring, reducing recovery time, and lowering medical costs [2]. However, despite these potential benefits, current minimally invasive surgery instruments lack adequate tool dexterity and workspace visualization. For example, current neuroendoscopes (e.g., Artemis™, BrainPath®) consist of a stiff metal cannula with limited dexterity. This setup requires surgeons to tilt and torque the cannula through a burr hole to visualize and evacuate the hematoma [20,21]. This approach leads to brain tissue damage, creating what is colloquially referred to as a "cone of destruction" [21,22]. Further, the endoscopic view is subject to

[1]Corresponding author.

Contributed by the Mechanisms and Robotics Committee of ASME for publication in the Journal of Mechanisms and Robotics. Manuscript received June 28, 2023; final manuscript received October 22, 2023; published online December 11, 2023. Assoc. Editor: Chin-Hsing Kuo.

visibility constraints caused by obstructing anatomy or bleeding. Poor visualization increases the risk of breaching the hemorrhagic cavity interface and suctioning normal tissue or surrounding vessels which could cause re-hemorrhage [23]. To improve endoscopic visualization, infusion of saline or gas is used to permit direct visualization of the cavity; however, this has the deleterious effect of concurrently increasing intracranial pressure and inducing aberrant neurotransmitter release [24,25].

Concentric tube robots (CTR) [26], a class of needle-sized robots made of multiple pre-curved elastic tubes [27,28], are a promising candidate for ICH evacuation due to their minimally invasive structure, their ability to navigate tortuous anatomy, and their pre-existing internal lumen for evacuation [29]. Additionally, CTRs are capable of deploying in a "follow-the-leader" fashion (i.e., the CTR traces the path of the tip throughout space over time), minimizing off-axis forces applied to surrounding healthy tissue and mitigating the cone of destruction [30,31]. Several groups have paired CTRs with appropriate imaging modalities to improve ICH evacuation and visualization. Burgner et al. developed a concentric tube robot for CT-guided ICH evacuation and validated the feasibility in a phantom model [32]. However, CT can involve significant radiation exposure, and thus, image feedback should be minimized during the procedure [33]. For example, the number of CT scans performed within one procedure is usually no more than 4–5 [34], precluding real-time intraoperative evacuation monitoring. Alternatively, magnetic resonance imaging (MRI) guidance can provide real-time imaging feedback without radiation exposure and has been used for intraoperative navigation/monitoring in various settings [35–38]. Recently, we proposed an MRI-compatible concentric tube robot for ICH evacuation. We developed the MRI-compatible robot hardware and performed a feasibility study in a 3 T MRI scanner. The results indicated that accurate targeting and intraoperative evacuation monitoring could be achieved with real-time MRI feedback [39,40]. However, despite these promising results, the optimal geometry design and path planning for concentric tube robot-enabled ICH evacuation have yet to be fully developed. Although various methods for needle path planning in neurosurgery have been proposed, these approaches are mostly designed for straight tools [41,42]. Furthermore, even when nonlinear paths are considered for CTRs, existing methods oversimplify the follow-the-leader deployment and limit the needle segments to planar curves [43–45]. To address these limitations, we propose a novel approach that models and optimizes CTR shapes with mechanics-based follow-the-leader constraints for CTR needle path planning in neurosurgery.

In this paper, we systematically investigate the geometrical design of concentric tube robots and trajectory planning for safe ICH evacuation by minimizing path-induced risk. Here, the risk is predominately determined by the damage to the surrounding white matter fiber tracts and intracerebral blood vessels. Both can be clearly visualized in customized MR imaging sequences, such as Diffusion Weighted Imaging (DWI) [46,47], and intracranial vessel wall (IVM) imaging [48,49]. We first propose a parametrization method to describe the CTR path. Then, a mathematical model is formulated to evaluate the risk value caused by the surgical path. Finally, we implement a convenient and highly accurate optimization algorithm [50], genetic algorithm, to perform the optimization study that investigates the optimal CTR geometry for arbitrary intracranial targeting. The paper is arranged as follows: Sec. 2 describes the path parameterization; Sec. 3 introduces the risk values and risk map generation for path optimization; Sec. 4 presents the path optimization method to determine the best geometry for CTR design; Sec. 5 concludes this article.

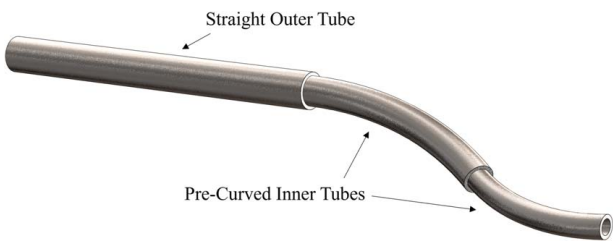

Fig. 1 Our CTR is consisted of a non-deformable straight tube as the outer tube and multiple pre-curved super-elastic inner tubes

2 Concentric Tube Robots Path Parametrization

In this section, we present our proposed CTR path parameters and compute the geometry of the CTR for targeting. The components of our CTR include a non-deformable straight tube as the outer tube and multiple pre-curved super-elastic inner tubes as shown in Fig. 1. The non-deformable straight tube is designed to penetrate through the burr hole in the skull, while the pre-curved inner tubes add dexterity to avoid high-risk regions. Herein, we intentionally choose helical tubes, which permit follow-the-leader deployment [30]. Consequently, the resultant shape of our CTR is a straight line followed by successive helices. In this section, we present the method of using one straight line S and $n-1$ helices H to represent a configuration of successive helices SH_{n-1}, providing a total of n path segments to construct a group of three-dimensional paths from the starting point to the target point. Since straight lines and planar curves are special forms of helices, the parametrization of n-connected helices (H_n) is proposed in this section.

2.1 Geometry Description of H_n. Before introducing our proposed parametrization method for H_n (i.e., n end-to-end helices, including the first straight tube), we begin by describing a single helix in space. Traditionally, a helical shape can be parameterized in the form $x=a\cos t,\ y=a\sin t,\ z=bt,\ a>0,\ t\in[0,\ T]$ which lies on a cylinder $x^2+y^2=a^2$ [51]. Specifically, the helix is right-handed with $b>0$, left-handed with $b<0$, and circular with $b=0$. However, this traditional expression only specifies the shape (radius, pitch, and length) of the helical arc, while omitting the helix origin and orientation. Thus, to fully define a series of connected helices in space, a new parametrization method that can directly specify the start position and orientation of the helix is proposed, as shown in Fig. 2.

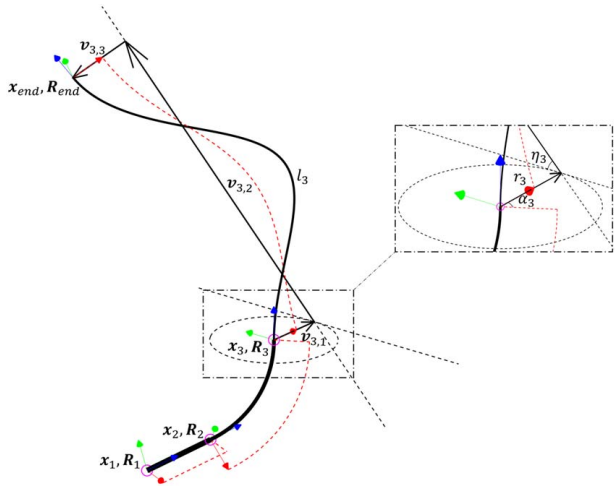

Fig. 2 Shape and configuration of SH_2. The red-green-blue (corresponding to *x*–*y*–*z* directions, respectively) coordinates represent starting position and orientation of each helical segment. The red dashed line indicates the imaginary trajectory of the orientation of the *x* direction about the helical centerline. The three black arrows are three vectors $v_{3,1}$, $v_{3,2}$, and $v_{3,3}$ connecting x_3 and x_{end}. Among these non-unit vectors, $v_{3,2}$ is colinear with the axis of the third segment of CTR, while $v_{3,1}$ and $v_{3,3}$ are both perpendicular to $v_{3,2}$.

For the ith helical segment of H_n, 5 parameters ($\boldsymbol{x}_i$, $\boldsymbol{R}_i$, l_i, r_i, and η_i) are needed to fully describe it, where $\boldsymbol{x}_i \in \mathbb{R}^3$ and $\boldsymbol{R}_i \in \mathrm{SO}(3)$ are the position and orientation of the ith helical segment starting point. l_i and r_i are the length and radius of the ith helical segment, and η_i is the slope angle of the helical segment. Besides, the sixth parameter α_i is a scalar to describe the relative rotation between two adjacent segments as shown in Fig. 1. The detailed definitions for these parameters are listed in Table 1.

With these parameters, $\boldsymbol{x}_{i+1}$ and $\boldsymbol{R}_{i+1}$, i.e., the starting position and orientation of the next helical segment, are fully determined as shown in Fig. 2. Thus, to obtain the starting pose ($\boldsymbol{x}_{i+1}$, $\boldsymbol{R}_{i+1}$) of a helical segment according to preceding segment starting pose ($\boldsymbol{x}_i$, $\boldsymbol{R}_i$), we have

$$\begin{cases} \boldsymbol{x}_{i+1} = \boldsymbol{x}_i + \boldsymbol{v}_{i,1} + \boldsymbol{v}_{i,2} + \boldsymbol{v}_{i,3} \\ \boldsymbol{R}_{i+1} = \mathrm{Rot}(\phi_i, \boldsymbol{v}_{i,2})\boldsymbol{R}_i \mathrm{Rot}(\alpha_i, \boldsymbol{z}) \end{cases} \tag{1}$$

where $\mathrm{Rot}(\theta, \boldsymbol{n}) = e^{\hat{\boldsymbol{n}}\theta}$ is an axis-angle represented rotation matrix and $\hat{\boldsymbol{n}}$ is the skew-symmetric matrix of $\boldsymbol{n}$. ϕ_i is the enwinding angle (i.e., the angle corresponding to the number of rotations) of the ith helical segment. The connected vectors $\boldsymbol{v}_{i,1}$, $\boldsymbol{v}_{i,2}$, and $\boldsymbol{v}_{i,3}$ ($v_{i,j}$ is the jth connected vector of the ith helical segment) are shown in Fig. 2.

For these intermediate variables, we have

$$\begin{cases} \boldsymbol{v}_{i,1} = \boldsymbol{R}_i \boldsymbol{u}_x r_i \\ \boldsymbol{v}_{i,2} = \boldsymbol{R}_i \mathrm{Rot}(\eta_i, \boldsymbol{u}_x)\boldsymbol{u}_y l_i \sin\eta_i \\ \boldsymbol{v}_{i,3} = -\boldsymbol{R}_i \mathrm{Rot}(\phi_i, \mathrm{Rot}(\eta_i, \boldsymbol{u}_x)\boldsymbol{u}_y)\boldsymbol{u}_x r_i \\ \phi_i = l_i \cos\eta_i / r_i \\ \boldsymbol{u}_x = \begin{bmatrix} 1 & 0 & 0 \end{bmatrix}^T \\ \boldsymbol{u}_y = \begin{bmatrix} 0 & 1 & 0 \end{bmatrix}^T \\ \boldsymbol{u}_z = \begin{bmatrix} 0 & 0 & 1 \end{bmatrix}^T \end{cases} \tag{2}$$

The aforementioned equations show that given $\boldsymbol{x}_i$, $\boldsymbol{R}_i$, α_i, l_i, r_i, and η_i, the shape of the ith helical segment and the starting position and orientation of the $i+1$ helical segment are fully determined. Thus, to parametrize a H_n path consisting of n helices, $4n+2$ parameters are needed: $\boldsymbol{x}_1, \boldsymbol{R}_1, \{l_1, l_2, \ldots l_n\}, \{r_1, r_2, \ldots, r_n\}, \{\eta_1, \eta_2, \ldots, \eta_n\}$, and $\{\alpha_1, \alpha_2, \ldots, \alpha_n\}$.

It should be noted that for a practical targeting problem, the distal tip of the path $\boldsymbol{x}_{\mathrm{end}}$ is given by the treatment target. To ensure the target $\boldsymbol{x}_{\mathrm{end}}$ is within the workspace of the tube path, the path parameters must be properly selected. In this paper, we replace the constraints $\{\eta_n, r_n, l_n\}$ with $\boldsymbol{x}_{\mathrm{end}}$ without changing the dimension of parameters. $\{\eta_n, r_n, l_n\}$ and $\boldsymbol{x}_{\mathrm{end}}$ can be related to each other based on the following equation:

$$r_n \begin{bmatrix} 1 - \cos\phi_n \\ (\phi_n - \sin\phi_n)\sin\eta_n \\ \dfrac{\sin^2\eta_n}{\cos\eta_n}(\phi_n - \sin\phi_n) + \dfrac{\sin\phi_n}{\cos\eta_n} \end{bmatrix} = \boldsymbol{R}_n^T(\boldsymbol{x}_{\mathrm{end}} - \boldsymbol{x}_n) \tag{3}$$

The detailed derivation and solution of Eq. (3) are given in the Appendix in Sec. 7. Thus, the parametrization method for a path defined by H_n segments that reaches target point $\boldsymbol{x}_{\mathrm{end}}$ is expressed by $\boldsymbol{x}_1, \boldsymbol{R}_1, \boldsymbol{x}_{\mathrm{end}}, \{l_1, l_2, \ldots l_{n-1}\}, \{r_1, r_2, \ldots, r_{n-1}\}, \{\eta_1, \eta_2, \ldots, \eta_{n-1}\}$, and $\{\alpha_1, \alpha_2, \ldots, \alpha_n\}$. Specifically, a CTR has the shape of SH_{n-1} meaning that the first segment of the needle path is a straight line S, and therefore, $\eta_1 = 0$, which leads to $r_1 = \infty$. To avoid introducing ∞, the curvature $\kappa_i = 1/r_i$ is used throughout the remainder of this paper in lieu of the radius r_i. Hence, the parameters for a SH_{n-1} path are $\boldsymbol{x}_1$, $\boldsymbol{R}_1$, $\boldsymbol{x}_{\mathrm{end}}$, $\{l_1, l_2, \ldots l_{n-1}\}$, $\{\kappa_2, \kappa_3, \ldots, \kappa_{n-1}\}$, $\{\eta_2, \eta_3, \ldots, \eta_{n-1}\}$, and $\{\alpha_1, \alpha_2, \ldots, \alpha_n\}$.

Table 1 Parameterization of the *i*th helix in H_n

Symbol	Field	Range	Description
$\boldsymbol{x}_i$	$\mathbb{R}^3$	N/A	Start position
$\boldsymbol{R}_i$	SO(3)	N/A	Start orientation
l_i	$\mathbb{R}$	$(0, \infty)$	Helix length
r_i	$\mathbb{R}$	$(0, \infty)$	Helix radius
η_i	$\mathbb{R}$	$(-\pi/2, \pi/2)$	Slope angle
α_i	$\mathbb{R}$	$(0, \pi)$	$\boldsymbol{R}_i$ Rotation angle

2.2 Follow-the-Leader Constraints for Concentric Tube Robots. A noteworthy feature of the proposed path parametrization method is that the identified path guarantees the target point $\boldsymbol{x}_{\mathrm{end}}$ is reached if the aforementioned equations are solvable. In this paper, we only consider CTR with $n \leq 3$, which are SH_0, SH_1, and SH_2. This is because more tubes could lead to significant challenges in robot hardware design, leading to limited feasibility in the practical operation scenarios. In addition, we assume that the outer straight tube is sufficiently rigid, such that we only consider the follow-the-leader deployment between two helical tubes for SH_2 configuration. According to Ref. [30], SH_2 configuration can satisfy this constraint if the path ensures the last two tubes are (1) planar circular curves that lie in the same plane or (2) helical segments that share a same torsion τ, defined as

$$\begin{cases} \alpha_3 - \alpha_2 = k\pi & (\eta_2 = \eta_3 = 0, k \in \mathbb{Z}) \\ \tau_2 = \tau_3 & (\eta_2 \neq 0, \eta_3 \neq 0) \end{cases} \tag{4}$$

where τ_i is the torsion of the ith helix. Torsion of a helix with the above parameterization is [51]

$$\tau_i = \frac{\tan\eta_i}{1 + \tan^2\eta_i}\kappa_i \tag{5}$$

Here, we divide the parametrization method into two conditions, $\eta_2 = \eta_3 = 0$ or $\eta_2 \neq 0$, $\eta_3 \neq 0$, meaning that the CTR shapes are a straight line followed by (1) two planar curved tubes or (2) two helical tubes, respectively. To distinguish them, we use SA_2 to denote the planar curved arc configuration. Accordingly, we use SA_1 to denote the CTR configuration with one straight tube followed by a single planar curved tube. We do not consider the situations that $\eta_2 = 0$, $\eta_3 \neq 0$ or $\eta_2 \neq 0$, $\eta_3 = 0$ in this paper.

For planar curved arc configurations, α_2 can be directly computed

$$\alpha_2 = \mathrm{atan}\,2(\boldsymbol{u}_y^T\boldsymbol{R}_1(\boldsymbol{x}_{\mathrm{end}} - \boldsymbol{x}_2), \boldsymbol{u}_x^T\boldsymbol{R}_1(\boldsymbol{x}_{\mathrm{end}} - \boldsymbol{x}_2)) \tag{6}$$

and α_3 can be obtained according to Eq. (4). For helical arc configurations, α_3 can be solved from Eq. (3). However, a simultaneous solution for Eqs. (3) and (4) is not always feasible, and an alternative equation is proposed to minimize the error of follow-the-leader deployment and to replace Eq. (4) with a numerical solution

$$\alpha_3 = \mathrm{argmin}(|\tau_2 - \tau_3|) \tag{7}$$

3 Path Risk Value Calculation

In this paper, two critical structures are considered for avoidance during the path-planning stage: the nerve fibers in white matter tracts and the cerebral arteries. The overarching goal is to mitigate the damage to selected nerve fibers and cerebral arteries during the procedure. In this section, we will detail the method to calculate the path risk value of a given path to evaluate the safety of a path.

3.1 Data Description and Visualization. Two critical structures, namely, the white matter tracts and cerebral arteries, are considered in the path planning algorithm. As shown in Table 2, eight tracts containing the most concerned nerve fibers are identified to be avoided. They were selected due to the direct correlation between subcortical strokes and these selected fibers [52–54]. However, more fibers can be considered per the physician's suggestions. The spatial representation of the tracts was adopted from the latest version of the tractography atlas developed by Yeh et al. [55]. The statistical atlas of Mouches et al. was used for the cerebral

Table 2 Selected tract

Tract number	Tract name
1	Anterior thalamic radiation
2	Corticospinal tract
3	Optic radiation
4	Arcuate fasciculus
5	Corpus callosum
6	Superior longitudinal fasciculus
7	Frontal aslant
8	Cingulum

arteries [56]. The hemorrhages are segmented from the MRI scans of anonymous patients provided by the clinical collaborators. Figure 3 presents a visualization of the nerve fibers in the eight selected tracts and the cerebral arteries. The central block represents the intracerebral hemorrhage.

3.2 Concentric Tube Robots Path Risk Value. The risk value of a CTR path is obtained via the following four steps: (1) Calculate $\mathrm{RV}_{\mathrm{fiber}}$, $\mathrm{RV}_{\mathrm{artery}}$, which are the risk value of a point $\boldsymbol{p} \in \mathbb{R}^3$ to an individual nerve fiber and artery, respectively; (2) Calculate $\mathrm{RV}_{\mathrm{fibers}}$, $\mathrm{RV}_{\mathrm{arteries}}$, which are the risk value of the point $\boldsymbol{p}$ to all fibers and arteries; (3) Calculate $\mathrm{RV}_{\mathrm{point}}$, which is the risk value of the point $\boldsymbol{p}$ by weighted summing $\mathrm{RV}_{\mathrm{fibers}}$ and $\mathrm{RV}_{\mathrm{arteries}}$, and the tissue damage risk term $\mathrm{RV}_{\mathrm{tissue}}$; (4) Calculate $\mathrm{RV}_{\mathrm{path}}$, which is the risk value of a CTR path summing $\mathrm{RV}_{\mathrm{point}}$ of all sampled points along the path.

As shown in Fig. 4, for an individual nerve fiber $\boldsymbol{Q}_k$, we define the following risk value at a point $\boldsymbol{p}$ as the sum of N_k (N_k is the number of sampled points of the kth fiber, decided by the length of the fiber) point-to-point risk values by uniformly sampling the kth fiber with N_k points $\boldsymbol{q}_{k,1}, \boldsymbol{q}_{k,2}, \ldots, \boldsymbol{q}_{k,N_k}$

$$\mathrm{RV}_{\mathrm{fiber}}(\boldsymbol{p}, \boldsymbol{Q}_k) = \sum_{i=1}^{N} rv(\|\delta_i\|) \tag{8}$$

$$rv(\delta) = \begin{cases} F(r;\delta,r) - F(-r;\delta,r) & \text{if } \delta < \delta_{\max} \\ 0 & \text{if } \delta \geq \delta_{\max} \end{cases} \tag{9}$$

where $\delta_i = \|\boldsymbol{p} - \boldsymbol{q}_{k,i}\|$ is the distance between $\boldsymbol{p}$ and the ith point ($\boldsymbol{q}_{k,i}$) along the fiber ($\boldsymbol{Q}_k$). $\delta_{\max}$ is the threshold distance of zero risk value. If $\delta_i > \delta_{\max}$, $rv(\delta_i) = 0$, meaning that $\boldsymbol{q}_{k,i}$ is too far from $\boldsymbol{p}$ to influence its risk value. If $\delta_i \leq \delta_{\max}$, the real distance δ_r between $\boldsymbol{p}$ and $\boldsymbol{q}_{k,i}$ is estimated to be of a normal distribution and risk value is the probability of $\delta_r < r$. We use probability to estimate risk value for two reasons: (1) rv(δ) can be interpreted as the probability of hitting the fiber with distance δ; (2) The changing trend of rv is monotonically decreasing. r is the cross-section radius of the CTR, and $\delta_{\max}$ is manually set to be $25r$ in this paper. The standard deviation σ of the normal distribution of the distance between $\boldsymbol{p}$ and $\boldsymbol{q}_{k,i}$ is taken as r for simulation, which can be substituted per physician's preference and patient-specific images. Hence, the risk value is $F(r;\delta_i, r) - F(-r;\delta_i, r)$, representing the probability of the point $\boldsymbol{p}$ damaging the fiber point $\boldsymbol{q}_{k,i}$. $F(x;\mu, \sigma)$ is the cumulative distribution function of normal distribution $X \sim N(\mu, \sigma)$.

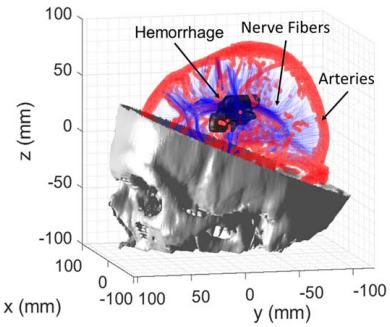

Fig. 3 Visualization of the selected nerve fibers, cerebral arteries, and the hemorrhage in the brain

After the risk value from a fiber to a point can be properly calculated, the risk value of all fibers to a point is the weighted sum of all individual fibers, as shown in Fig. 4

$$\mathrm{RV}_{\mathrm{fibers}}(\boldsymbol{p}, [\boldsymbol{Q}_1, \boldsymbol{Q}_2, \ldots \boldsymbol{Q}_M]) = \sum_{k=1}^{M} \mathrm{RV}_{\mathrm{fiber}}(\boldsymbol{p}, \boldsymbol{Q}_k) f_k \tag{10}$$

where $\boldsymbol{Q}_k = [\boldsymbol{q}_{k,1}, \boldsymbol{q}_{k,2}, \ldots, \boldsymbol{q}_{k,N_k}]$ is a matrix of N_k points sampled from the kth fiber. f_k is the weight of fibers. Note that all weights are 1 in this paper, i.e., $f_1 = f_2 = \cdots = f_M = 1$, indicating that all the fibers have equal importance, but can be changed per surgeon's input and patient-specific hematoma location.

For the arteries, the risk value $\mathrm{RV}_{\mathrm{arteries}}$ at a point is computed in a similar manner to the nerve fiber risk calculation. However, to emphasize the priority of protecting arteries over the fibers, the weighted sum of $\mathrm{RV}_{\mathrm{fibers}}$ and $\mathrm{RV}_{\mathrm{arteries}}$ is introduced

$$\mathrm{RV}_{fa}(\boldsymbol{p}) = w\mathrm{RV}_{\mathrm{fibers}} + (1-w)\mathrm{RV}_{\mathrm{arteries}} \tag{11}$$

where w is a scalar weighting $\mathrm{RV}_{\mathrm{fibers}}$ and $\mathrm{RV}_{\mathrm{arteries}}$ and is chosen to be $w < 0.5$ in this paper, meaning that the risk of damaging arteries is more important than the fibers as transecting arteries can potentially cause new hemorrhages.

The damage to brain tissue other than nerve fibers and arteries is also considered by adding a term $\mathrm{RV}_{\mathrm{tissue}}$, determined by the mean value of $\mathrm{RV}_{fa}(\boldsymbol{p})$ for all the n sample points in the brain

$$\mathrm{RV}_{\mathrm{tissue}} = \frac{1}{n}\sum_{i=1}^{n} \varepsilon \mathrm{RV}_{fa}(\boldsymbol{p}_i) \tag{12}$$

where ε is a positive constant value controlling the size of $\mathrm{RV}_{\mathrm{tissue}}$, which represents the inherent risk associated with all sample points. ε should be small ($\varepsilon < 0.1$), indicating the damage to other tissues is trivial compared to fibers or arteries. Thus, the final risk value of a point of interest is

$$\mathrm{RV}_{\mathrm{point}}(\boldsymbol{p}) = \mathrm{RV}_{fa}(\boldsymbol{p}) + \mathrm{RV}_{\mathrm{tissue}} \tag{13}$$

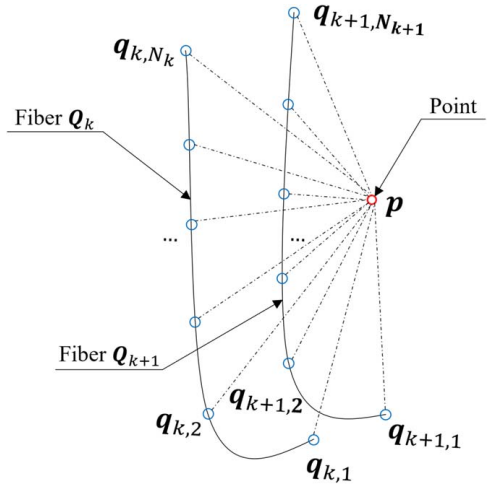

Fig. 4 Illustration of computing $\mathrm{RV}_{\mathrm{fiber}}$ and $\mathrm{RV}_{\mathrm{fibers}}$. The solid black lines are nerve fibers Q_k and Q_{k+1}, with sampled points $q_{k,1} \cdots q_{k,N_k}$ and $q_{k+1,1} \cdots q_{k+1,N_{k+1}}$. The risk value of point p with respect to the nerve fibers is the sum of all risk values between p and sampled points q, as shown by the dashed lines in the figure.

And the risk value of a CTR tube path is the sum of the risk values of all sample points along the path

$$\mathrm{RV}_{\mathrm{path}}(\boldsymbol{p}_1, \boldsymbol{p}_2, \ldots, \boldsymbol{p}_L) = \sum_{i=1}^{L} \mathrm{RV}_{\mathrm{point}}(\boldsymbol{p}_i) \tag{14}$$

where $\boldsymbol{p}_1, \boldsymbol{p}_2, \ldots, \boldsymbol{p}_L$ are L points sampled from the parameterized CTR path. The arc length between two sample points is constant, which is equal to tube radius r in the preliminary study.

It should be noted that without the introduction of the term $\mathrm{RV}_{\mathrm{tissue}}$ (i.e., $\varepsilon = 0$), the optimization of the CTR path based on $\mathrm{RV}_{fa}(\boldsymbol{p})$ does not provide a reasonable solution, as all path points with the distance to its nearest fiber point neighbor larger than $\delta_{\max}$ share the same risk value 0. Thus, the length of the path cannot be controlled without $\mathrm{RV}_{\mathrm{tissue}}$. This is further explained in Fig. 5, where Path I and Path II have the same $\mathrm{RV}_{\mathrm{path}}$ value 0.

3.3 3D Risk Map. For a given cerebral model, the risk values RV_{fa} for all sample points in the space can be precalculated to obtain a three-dimensional risk map, which can serve as a lookup table to simplify the computation of $\mathrm{RV}_{\mathrm{path}}$ during the path planning and optimization procedure. Here, we create a risk map of RV_{fa} for the brain model by repeating the process from Eqs. (8)–(12) and calculate RV_{fa} for $171 \times 278 \times 245$ sample points in the brain model, with the sampling resolution 1 mm × 1 mm × 1 mm, i.e., $r \times r \times r$. Figure 6 depicts the risk map of the left brain in the plane of $z = 40$ mm. As the figure illustrates, the peaks of the risk value (red) appear near fiber-dense area or near-arterial regions, whereas the regions far from the nerve fibers have significantly low-risk values (blue). The region, which does not intersect with the nerve fibers or arteries, but is sufficiently close to them, has a relatively lower risk value than the higher risk region.

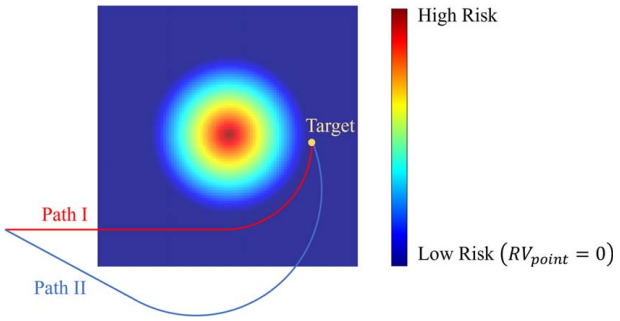

Fig. 5 Path I and Path II have the same path risk value $\mathrm{RV}_{\mathrm{path}}$ of 0 since they are all away from the high-risk region. Hence, Path II cannot be optimized towards Path I and the length of the CTR path is not controlled when $\varepsilon = 0$.

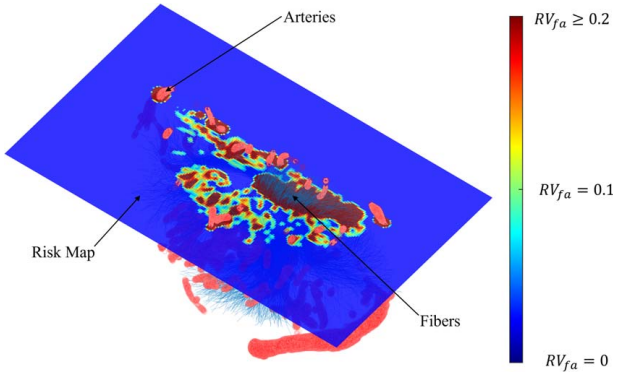

Fig. 6 Visualization of a risk map at the plane $z = 40$ mm. It can be seen that regions near fibers and arteries are assigned higher risk values. In this simulation, we assume $w = 0.1$.

4 Optimal Concentric Tube Robots Path Planning

4.1 Optimization of Concentric Tube Robots Path. This section details the method to determine the optimal number and shape of a CTR for reaching an arbitrary target. Here, we limit the number of tubes to three to simplify the follow-the-leader criteria and analyze current common CTR configurations. The corresponding paths for three-tube CTR designs are SH_0, SA_1, SH_1, SA_2, and SH_2 (S represents the path shape beginning with a straight tube, and H_i or A_i represents i number of helical or planar curved tubes, respectively). Here, we would like the emphasize that H_0 is a straight line, which will be used as the control data. We use a genetic algorithm with the same hyperparameters to optimize the paths to reach a total number of 100 target points randomly generated inside half of the brain ($y \geq 0$, where y is the coordinate corresponding to the origin $\boldsymbol{O}$ as shown in Fig. 7, which is the centroid of the skull model). We only generate target points in half of the brain because we assume the geometry of the brain fibers, cerebral arteries, and other structures are approximately symmetrical (about the xz plane) [57]. Moreover, the position and direction of an entry point ($\boldsymbol{x}_1$ and $\boldsymbol{R}_1$) is also limited to half of the skull at the same side of the target points. This will rule out infeasible solutions (e.g., a path starting from one side of the brain, and penetrating through the brain to reach the target points on the opposite side).

As shown in Fig. 7, the starting point $\boldsymbol{x}_1$ can be determined by β and γ, which parameterizes a straight line L starting from the origin $\boldsymbol{O}$ (center of the skull) to the skull's exterior surface. The point $\boldsymbol{x}_1$ is the intersection of the line and the surface. The starting direction $\boldsymbol{R}_1$ can be determined by the deviation angle β_d and γ_d and the normal direction unit vector $\boldsymbol{z}_{nm}$, which can be computed from the skull model shown in Fig. 7. To get the insertion orientation, $\boldsymbol{R}_{nm}$, $\boldsymbol{x}_{nm}$ and $\boldsymbol{y}_{nm}$ are introduced

$$\boldsymbol{y}_{nm} = \frac{\boldsymbol{u}_z \times \boldsymbol{z}_{nm}}{\boldsymbol{u}_z \times \boldsymbol{z}_{nm}} \tag{15}$$

$$\boldsymbol{x}_{nm} = \boldsymbol{y}_{nm} \times \boldsymbol{z}_{nm} \tag{16}$$

$$\boldsymbol{R}_{nm} = \begin{bmatrix} \boldsymbol{x}_{nm} & \boldsymbol{y}_{nm} & \boldsymbol{z}_{nm} \end{bmatrix} \tag{17}$$

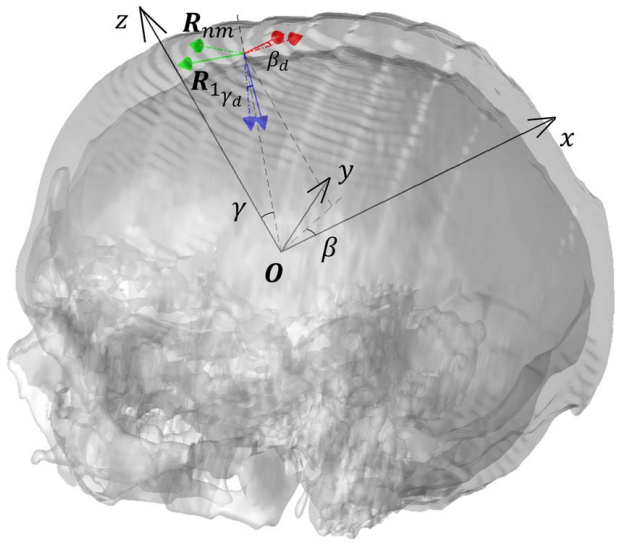

Fig. 7 Entry point and starting direction in a global frame with origin O. The dash-dotted coordinate is the normal orientation R_{nm} with the z-axis perpendicular to the skull surface and y-axis pointing to the global z-axis. The solid coordinate is the starting orientation R_1 of CTR with deviation angles β_d and γ_d to R_{nm}.

Thus, as shown in Fig. 7, the insertion direction $\boldsymbol{R}_1$ can be specified by

$$\boldsymbol{R}_1 = \boldsymbol{R}_{nm}\text{Rot}(\gamma_d, \boldsymbol{u}_z)\text{Rot}(\beta_d, \boldsymbol{u}_x) \tag{18}$$

Hence, $\boldsymbol{x}_1$ and $\boldsymbol{R}_1$ are substituted for path parametrization and the final input vectors for the genetic algorithm are

$$\begin{cases} \boldsymbol{v}_{SH_0} = [\beta, \gamma] \\ \boldsymbol{v}_{SA_1} = [\beta, \gamma, \beta_d, \gamma_d, \alpha_1, l_1] \\ \boldsymbol{v}_{SH_1} = [\beta, \gamma, \beta_d, \gamma_d, \alpha_1, l_1, \alpha_2] \\ \boldsymbol{v}_{SA_2} = [\beta, \gamma, \beta_d, \gamma_d, \alpha_1, l_1, \kappa_2, l_2] \\ \boldsymbol{v}_{SH_2} = [\beta, \gamma, \beta_d, \gamma_d, \alpha_1, l_1, \alpha_2, \kappa_2, \eta_2, l_2] \end{cases} \tag{19}$$

Notice that the target point $\boldsymbol{x}_{\text{end}}$ does not appear in Eq. (19) since $\boldsymbol{x}_{\text{end}}$ will be constant once the target is selected. The genetic algorithm only needs to optimize the parameters in Eq. (19) to reduce the risk value of the path. The parameters and constraints for the genetic optimization algorithm are summarized in Table 3.

Intuitively, the fitness value of genetic algorithm is the risk value of a CTR path RV_{path}. However, when solving Eq. (7) to satisfy the follow-the-leader constraint in the optimization process for an SH_2 configuration, it cannot guarantee the difference of torsion $|\tau_3 - \tau_2|$ to be exactly zero; i.e., the path is perfectly following the leader. To compensate for this, the objective function of the genetic algorithm is updated as follows:

$$f_{\text{obj}} = \begin{cases} \text{RV}_{\text{path}} + \rho|\tau_3 - \tau_2| & (\text{Shape is SH}_2) \\ \text{RV}_{\text{path}} & (\text{Other Shapes}) \end{cases} \tag{20}$$

where ρ is a coefficient weighting the difference between the torsions of two helical tubes in SH_2. It is noteworthy that ρ is only introduced for SH_2 configurations.

To find the best ρ value that can reduce path risk value with relatively low $|\tau_3 - \tau_2|$, we vary ρ from 0 to 20 and obtain the results shown in Fig. 8. The results indicate that a reasonable ρ value can lead to a smaller difference between τ_2 and τ_3 without significantly affecting path risk value. According to Fig. 8, we choose ρ to be 10 for all SH_2 path optimization configurations in this paper.

5 Results

To evaluate the risk values of five different geometrical designs, we compared the mean risk value of 100 optimized paths for the same set of targets with the path shape being SH_0, SA_1, SH_1, SA_2, and SH_2. The value of w (the weight between $\text{RV}_{\text{fibers}}$ and $\text{RV}_{\text{arteries}}$) is set to 0.1, 0.2 and 0.3 to get three data groups as shown in Fig. 9.

From Fig. 8 and Table 4, it is shown that the introduction of planar curved (SA_1, SA_2) or helical (SH_1, SH_2) tubes can efficiently reduce the risk value of the path compared to one obtained with SH_0. On average, the risk value can be reduced from a range of 83.4–84.2% for different w values. This is primarily due to the improved system dexterity provided by additional curved tubes, enabling safe paths toward the target while minimizing the damage to the surrounding obstacles (i.e., white fiber tracts and blood vessels). Comparing the helical tube configurations to the planar curved ones, we can conclude that the robot with helical tubes (SH_1, SH_2) can achieve a slightly lower risk value. This is likely due to the increased dexterity provided by helical tubes compared to the planar curved tubes. This can be further explained by the mathematical formulation of helical and planar curved arcs, where more parameters are required in the complete definition of the helical arc, providing additional parameters for defining a

Table 3 Parameters of the model

Items	Parameters	Values/Ranges
Path	r	1 mm
	ε	0.01
GA input vector	β	$[0, \pi]$
	γ	$[0, \pi/6]$
	β_d	$[-\pi, \pi]$
	γ_d	$[0, \pi/4]$
	α_1, α_2	$[0, \pi]$
	κ_2	$[-0.2, 0.2]$
	η_2	$[-\pi/2, \pi/2]$
	l_1	[10 mm, 80 mm]
	l_2	[0, 80 mm]
Genetic algorithm	Generations	25
	Population size	1000

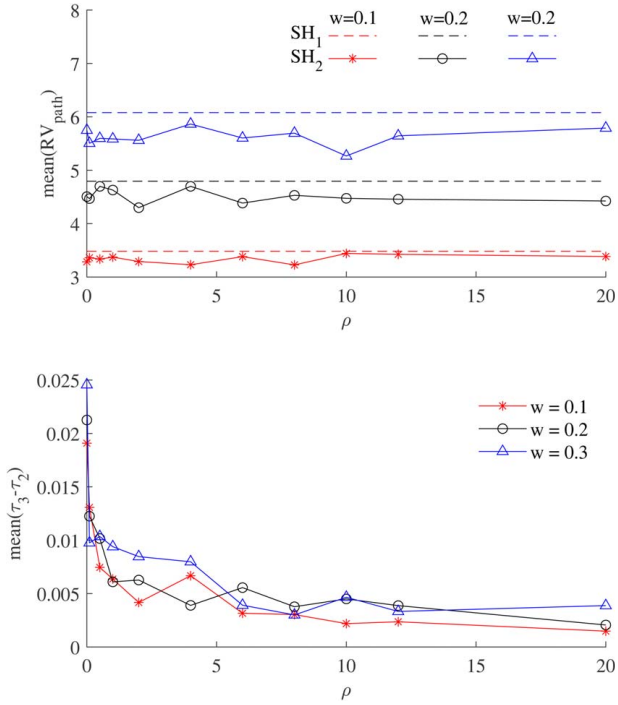

Fig. 8 For all w values (0.1, 0.2, and 0.3), average $|\tau_3 - \tau_2|$ value for 100 random cerebral targets decays exponentially as ρ increases. Additionally, the average path risk value RV_{path} in the SH_2 configuration is not significantly influenced as ρ increases.

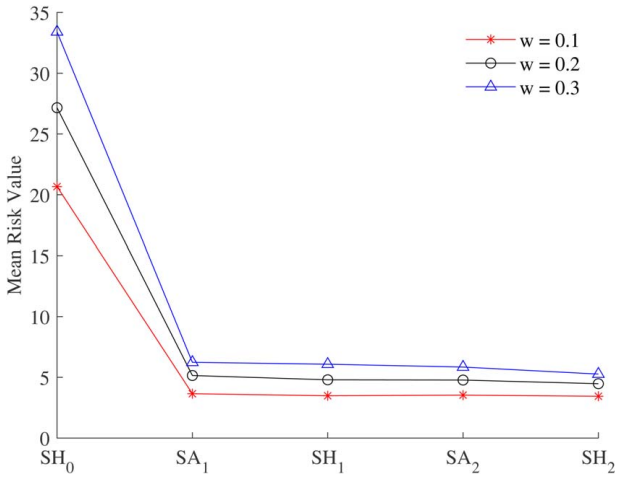

Fig. 9 Mean risk values for optimized paths with different shapes

Table 4 Mean risk values with different path geometries

	Mean(RV_{path})				
	SH_0	SA_1	SH_1	SA_2	SH_2
$w = 0.1$	20.667	3.650	3.482	3.534	3.442
$w = 0.2$	27.160	5.149	4.800	4.775	4.475
$w = 0.3$	33.403	6.234	6.078	5.844	5.267

safer path. For the same reason, multiple inner tube CTRs (SA_2, SH_2) are more dexterous than single inner tube CTRs (SA_1, SH_1) and provide additional tunable parameters. Thus, multiple inner tube CTRs can provide lower risk values. Additionally, it is noteworthy that the risk values are lower with smaller w values since fibers have a higher density within the brain compared to arteries, and hence, most path risk values are mainly dominated by the fibers.

By analyzing the actual optimized paths of CTR as shown in Figs. 10 and 11, we note that the risk value improvement depends on the target locations within the brain. As can be seen in Fig. 10, the introduced arcs do not lead to an obvious improvement in the damage ratio (2.4–6.7%) when the targets are located superficially in the brain. When the targets are located deeper inside the brain, the dexterity of the multi-tube designs can contribute to significant damage reduction, as shown in Fig. 10. We selected three scenarios here to show that the improvement of damage ratio can be significant (36% versus 83%). However, Fig. 9 also indicates that the damage reduction from single inner tube designs to multiple inner tube designs is not significant (3.2–6.3% for SA_1 to SA_2 and 1.2–6.8% for SH_1 to SH_2). With our cerebral model being sparse in space (most of the cerebral space is not occupied by fibers or arteries), the extra segment of the needle tube is redundant for reaching most targets, and the second segment of the CTR is optimized to be short and neglectable as shown in Fig. 11, leading to the similar risk value obtained between SA_1 and SA_2, SH_1 and SH_2, respectively.

Another important conclusion, we want to highlight is that there is no significant difference between the helical tube and planar curved tube designs. Only a trivial damage reduction can be obtained from SA_1 to SH_1 (2.5–6.8%) or from SA_2 to SH_2 (2.6–9.9%). The main reason is that the spatial distribution of the chosen neural fibers and cerebral arteries in our model is concentrated in certain regions. Thus, the simple planar curved tube design can enable the CTR to reach most targets among 100 random points safely without increasing the high-risk value by avoiding these congested regions. As shown in Figs. 11(*b*) and 11(*c*), the optimized SA_1 and SH_1 paths tend to achieve similar performance, indicating that helical tubes behave like planar curved tubes and minimize path length. Further, the extra torsional dimension of helical tubes does not provide any prominent improvement to the damage ratio. Despite the minor improvement in risk values with the use of helical tubes, the planar curved tubes are much easier for fabrication, robot design, and control. Thus, taking all the aforementioned factors into consideration, we can conclude that the CTR with SA_1 is the most feasible solution compared to other tube geometries mentioned in this paper.

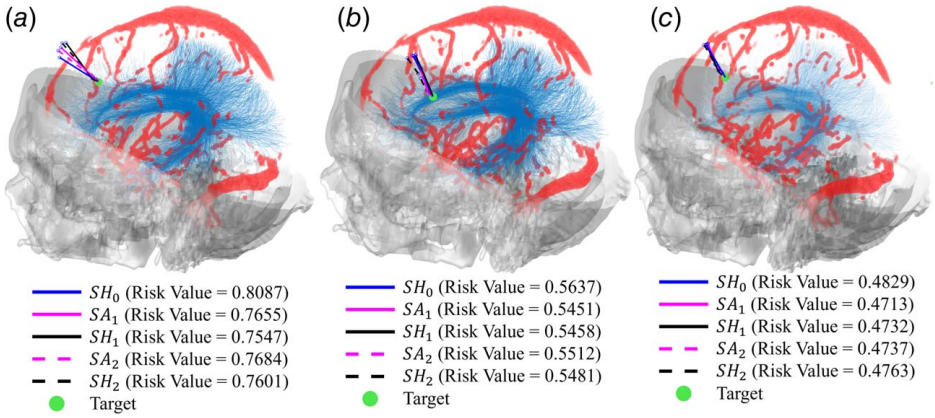

Fig. 10 In these scenarios, the difference between the risk values (listed on in-figure labels) of SH_0 and other geometries is not significant since the target is near the surface of the brain and all paths are comparable

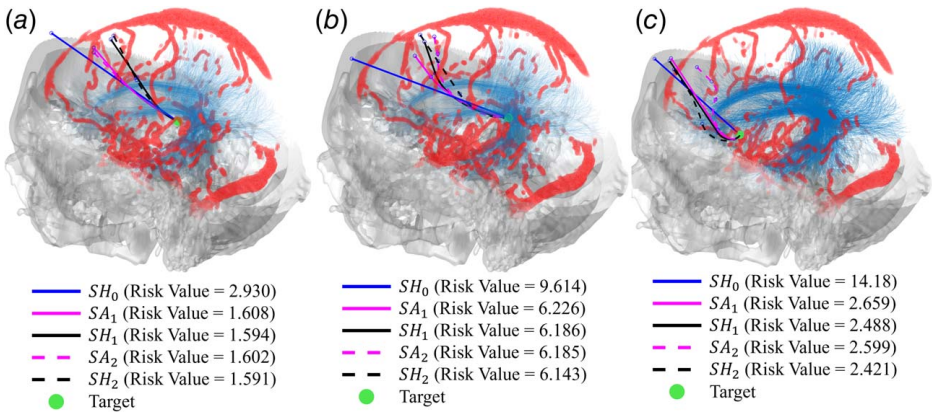

Fig. 11 For (*a*) and (*b*), the length of second segments of SA_2 and SH_2 is neglectable and the geometry resembles to SA_1 or SH_1. For (*b*) and (*c*), SA_1 and SH_1 paths are proximal to each other and the paths with helical tubes provide a trivial decrease in risk value compared to planar-curved-tube-only solutions.

6 Conclusion

In this article, we proposed the optimal design and path planning for CTR-enabled ICH removal. The CTR design starts with five potential solutions, which include SH_0, SH_1, SH_2, SA_1, and SA_2, which represents a straight path, a straight path with one helical segment, a straight path with two helical segments, a straight path with one planar curved segment, and a straight path with two planar curved segments, respectively. A custom-defined risk value is proposed to minimize the damage to nerve fibers, arteries, and total needle insertion distance. The optimal CTR design is searched using the genetic algorithm that minimizes the risk value among 100 targets inside the brain. The results indicate that the introduction of curved tubes (either planar curved tubes or helical tubes) can significantly minimize the risk value compared to the one obtained with the conventional straight tube. There is no significant difference between the number (1 or 2) and shape (planar curved or helical) of the introduced inner tubes. Considering the practical challenges in CTR hardware design, fabrication, and control, we conclude that the CTR with a planar curved inner tube is the preferred design for the proposed ICH evacuation procedure. Our future work will focus on integrating the global path plan method proposed in this paper with our TSGP controller [58] and implementing it on our ICH evacuation robot.

Acknowledgment

The authors would like to thank Cosmo Xiao for performing the preliminary analysis.

Funding Data

- This project was funded by the Georgia Tech McCamish Blue Sky Grant. Research reported in this publication was also supported by the National Institute of Neurological Disorders and Stroke of the National Institutes of Health under Award Number R01NS116148. The content is solely the responsibility of the authors and does not necessarily represent the official views of the National Institutes of Health.

Conflict of Interest

There are no conflicts of interest.

Data Availability Statement

No data, models, or code were generated or used for this paper.

Appendix

As shown in Fig. 2, the target point $\boldsymbol{x}_{\text{end}}$ is connected to the starting point of the nth tube $\boldsymbol{x}_n$ by three intermediate vectors

$$\boldsymbol{x}_{\text{end}} - \boldsymbol{x}_n = \boldsymbol{v}_{n,1} + \boldsymbol{v}_{n,2} + \boldsymbol{v}_{n,3} \tag{A1}$$

According to Eq. (2)

$$\begin{cases} \boldsymbol{R}_n \boldsymbol{u}_x r_n = \boldsymbol{v}_{n,1} \\ \boldsymbol{R}_n \text{Rot}(\eta_n, \boldsymbol{u}_x)\boldsymbol{u}_y l_n \sin\eta_n = \boldsymbol{v}_{n,2} \\ -\boldsymbol{R}_n \text{Rot}(\phi_n, \text{Rot}(\eta_n, \boldsymbol{u}_x)\boldsymbol{u}_y)\boldsymbol{u}_x r_n = \boldsymbol{v}_{n,3} \\ l_n = r_n \phi_n / \cos\eta_n \end{cases} \tag{A2}$$

After substituting relative variables in Eq. (A1) using Eq. (A2), the following equation can be derived

$$\begin{aligned} &\boldsymbol{u}_x + \text{Rot}(\eta_n, \boldsymbol{u}_x)\boldsymbol{u}_y \phi_n \tan\eta_n - \text{Rot}(\phi_n, \text{Rot}(\eta_n, \boldsymbol{u}_x)\boldsymbol{u}_y)\boldsymbol{u}_x \\ &\quad = \boldsymbol{R}_n^T(\boldsymbol{x}_{\text{end}} - \boldsymbol{x}_n)/r_n \end{aligned} \tag{A3}$$

Then, Eq. (A3) can be simplified to the following form:

$$r_n \begin{bmatrix} 1 - \cos\phi_n \\ (\phi_n - \sin\phi_n)\sin\eta_n \\ \dfrac{\sin^2\eta_n}{\cos\eta_n}(\phi_n - \sin\phi_n) + \dfrac{\sin\phi_n}{\cos\eta_n} \end{bmatrix} = \boldsymbol{R}_n^T(\boldsymbol{x}_{\text{end}} - \boldsymbol{x}_n) \tag{A4}$$

Equation (A4) is Eq. (3) mentioned in Sec. 2. Furthermore, to solve r_n, ϕ_n, and η_n from $\boldsymbol{x}_n$, $\boldsymbol{R}_n$ and $\boldsymbol{x}_{\text{end}}$ in Eq. (A4), we assume that

$$\boldsymbol{R}_n^T(\boldsymbol{x}_{\text{end}} - \boldsymbol{x}_n) = \begin{bmatrix} \lambda \\ a\lambda \\ ab\lambda \end{bmatrix} \tag{A5}$$

Thus, r_n can be eliminated to get the following equation:

$$\begin{cases} \dfrac{\phi_n - \sin\phi_n}{1 - \cos\phi_n}\sin\eta_n = a \\ \tan\eta_n + \dfrac{\sin\phi_n}{(\phi_n - \sin\phi_n)\sin\eta_n \cos\eta_n} = b \end{cases} \tag{A6}$$

Then, Eq. (A6) can be simplified to the following form:

$$\begin{aligned} &\left(\frac{a(1-\cos\phi_n)}{b(\phi_n - \sin\phi_n)}\right)^2 (1 - b^2) + \left(\frac{\sin\phi_n}{ab(1-\cos\phi_n)}\right)^2 \\ &\quad + \frac{2\sin\phi_n}{b^2(\phi_n - \sin\phi_n)} = 0 \end{aligned} \tag{A7}$$

Note that solving for Eq. (A7) can lead to multiple solutions. We intuitively hypothesized that the optimized solution is the minimum absolute value of ϕ_n^* to exclude unreasonable solutions where the helical segment wraps around the axis for multiple revolutions. Thus, ϕ_n can be numerically solved from Eq. (A7). Then, η_n and r_n can be solved according to Eqs. (A6) and (A4).

References

[1] Poon, M. T. C., Fonville, A. F., and Al-Shahi Salman, R., 2014, "Long-Term Prognosis After Intracerebral Haemorrhage: Systematic Review and Meta-Analysis," J. Neurol. Neurosurg. Psychiatry, **85**(6), pp. 660–667.

[2] Wang, W., Zhou, N., and Wang, C., 2017, "Minimally Invasive Surgery for Patients With Hypertensive Intracerebral Hemorrhage With Large Hematoma Volume: A Retrospective Study," World Neurosurg., **105**, pp. 348–358.

[3] Fiorella, D., Zuckerman, S. L., Khan, I. S., Ganesh Kumar, N., and Mocco, J., 2015, "Intracerebral Hemorrhage: A Common and Devastating Disease in Need of Better Treatment," World Neurosurg., **84**(4), pp. 1136–1141.

[4] Maira, G., Anile, C., Colosimo, C., and Rossi, G. F., 2002, "Surgical Treatment of Primary Supratentorial Intracerebral Hemorrhage in Stuporous and Comatose Patients," Neurol. Res., **24**(1), pp. 54–60.

[5] Hanley, D. F., Thompson, R. E., Muschelli, J., Rosenblum, M., McBee, N., Lane, K., Bistran-Hall, A. J., et al., 2016, "Safety and Efficacy of Minimally Invasive Surgery Plus Alteplase in Intracerebral Haemorrhage Evacuation (MISTIE): A Randomised, Controlled, Open-Label, Phase 2 Trial," Lancet Neurol., **15**(12), pp. 1228–1237.

[6] Zuccarello, M., Brott, T., Derex, L., Kothari, R., Sauerbeck, L., Tew, J., Van Loveren, H., et al., 1999, "Early Surgical Treatment for Supratentorial Intracerebral Hemorrhage: A Randomized Feasibility Study," Stroke, **30**(9), pp. 1833–1839.

[7] Teernstra, O. P. M., Evers, S., Lodder, J., Leffers, P., Franke, C., and Blaauw, G., 2003, "Stereotactic Treatment of Intracerebral Hematoma by Means of a Plasminogen Activator: A Multicenter Randomized Controlled Trial (SICHPA)," Stroke, **34**(4), pp. 968–974.

[8] Kim, Y. Z., and Kim, K. H., 2009, "Even in Patients With a Small Hemorrhagic Volume, Stereotactic-Guided Evacuation of Spontaneous Intracerebral Hemorrhage Improves Functional Outcome," J. Korean Neurosurg. Soc., **46**(2), p. 109.

[9] Sun, H., Liu, H., Li, D., Liu, L., Yang, J., and Wang, W., 2010, "An Effective Treatment for Cerebral Hemorrhage: Minimally Invasive Craniopuncture Combined With Urokinase Infusion Therapy," Neurol. Res., **32**(4), pp. 371–377.

[10] Wang, W.-Z., Jiang, B., Liu, G.-M., Li, D., Lu, C.-Z., Zhao, Y.-D., and Sander, J., 2009, "Minimally Invasive Craniopuncture Therapy vs. Conservative Treatment for Spontaneous Intracerebral Hemorrhage: Results From a Randomized Clinical Trial in China," Int. J. Stroke, **4**(1), pp. 11–16.

[11] Zhou, H., Zhang, Y., Liu, L., Han, X., Tao, Y., Tang, Y., Hua, W., Xue, J., and Dong, Q., 2011, "A Prospective Controlled Study: Minimally Invasive Stereotactic Puncture Therapy Versus Conventional Craniotomy in the Treatment of Acute Intracerebral Hemorrhage," BMC Neurol., **11**(1), pp. 1–8.

[12] Yang, G., and Shao, G., 2016, "Clinical Effect of Minimally Invasive Intracranial Hematoma in Treating Hypertensive Cerebral Hemorrhage," Pak. J. Med. Sci., **32**(3), p. 677.
[13] Vespa, P., Hanley, D., Betz, J., Hoffer, A., Engh, J., Carter, R., Nakaji, P., et al., 2016, "ICES (Intraoperative Stereotactic Computed Tomography-Guided Endoscopic Surgery) for Brain Hemorrhage: A Multicenter Randomized Controlled Trial," Stroke, **47**(11), pp. 2749–2755.
[14] Miller, C. M., Vespa, P., Saver, J. L., Kidwell, C. S., Carmichael, S. T., Alger, J., Frazee, J., et al., 2008, "Image-Guided Endoscopic Evacuation of Spontaneous Intracerebral Hemorrhage," Surg. Neurol., **69**(5), pp. 441–446.
[15] Auer, L. M., Deinsberger, W., Niederkorn, K., Gell, G., Kleinert, R., Schneider, G., Holzer, P., et al., 1989, "Endoscopic Surgery Versus Medical Treatment for Spontaneous Intracerebral Hematoma: A Randomized Study," J. Neurosurg., **70**(4), pp. 530–535.
[16] Zhang, H.-Z., Li, Y.-P., Yan, Z.-C., Wang, X.-D., She, L., Wang, X.-D., and Dong, L., 2014, "Endoscopic Evacuation of Basal Ganglia Hemorrhage via Keyhole Approach Using an Adjustable Cannula in Comparison With Craniotomy," BioMed Res. Int., **2014**, pp. 1–6.
[17] Feng, Y., He, J., Liu, B., Yang, L., and Wang, Y., 2016, "Endoscope-Assisted Keyhole Technique for Hypertensive Cerebral Hemorrhage in Elderly Patients: A Randomized Controlled Study in 184 Patients," Turk. Neurosurg., **26**(1), pp. 84–89.
[18] Hattori, N., Katayama, Y., Maya, Y., and Gatherer, A., 2004, "Impact of Stereotactic Hematoma Evacuation on Activities of Daily Living During the Chronic Period Following Spontaneous Putaminal Hemorrhage: A Randomized Study," J. Neurosurg., **101**(3), pp. 417–420.
[19] Cho, D.-Y., Chen, C.-C., Chang, C.-S., Lee, W.-Y., and Tso, M., 2006, "Endoscopic Surgery for Spontaneous Basal Ganglia Hemorrhage: Comparing Endoscopic Surgery, Stereotactic Aspiration, and Craniotomy in Noncomatose Patients," Surg. Neurol., **65**(6), pp. 547–555.
[20] Bajaj, J., Yadav, Y. R., Pateriya, A., Parihar, V., Ratre, S., and Dubey, A., 2017, "Indigenous Inexpensive Practice Models for Skill Development in Neuroendoscopy," J. Neurosci. Rural Pract., **8**(2), pp. 170–173.
[21] Wang, W.-H., Hung, Y.-C., Hsu, S. P., Lin, C.-F., Chen, H.-H., Shih, Y.-H., and Lee, C.-C., 2015, "Endoscopic Hematoma Evacuation in Patients With Spontaneous Supratentorial Intracerebral Hemorrhage," J. Chin. Med. Assoc., **78**(2), pp. 101–107.
[22] Fukuhara, A., Tsujita, T., Sase, K., Konno, A., Nakagawa, A., Endo, T., Tominaga, T., Jiang, X., Abiko, S., and Uchiyama, M., 2016, "Securing an Optimum Operating Field Without Undesired Tissue Damage in Neurosurgery," Adv. Robot. Syst., **30**(19), pp. 1245–1259.
[23] Zhang, Y., Shan, A.-J., Peng, Y.-P., Lei, P., Xu, J., Zhong, X., and Du, B., 2019, "The Intra-Neuroendoscopic Technique (INET): A Modified Minimally Invasive Technique for Evacuation of Brain Parenchyma Hematomas," World J. Emerg. Surg., **14**(1), p. 21.
[24] Trnovec, S., Halatsch, M.-E., Putz, M., Behnke-Mursch, J., and Mursch, K., 2012, "Irrigation Can Cause Prolonged Intracranial Pressure Elevations During Endoscopic Treatment of Intraventricular Haematomas," Br. J. Neurosurg., **26**(2), pp. 247–251.
[25] Hannah, T. C., Kellner, R., and Kellner, C. P., 2021, "Minimally Invasive Intracerebral Hemorrhage Evacuation Techniques: A Review," Diagnostics, **11**(3), p. 576.
[26] Gilbert, H. B., Rucker, D. C., and Webster, R. J. III, 2016, "Concentric Tube Robots: The State of the Art and Future Directions," Rob. Res., **114**, pp. 253–269.
[27] Thomas, T. L., Kalpathy Venkiteswaran, V., Ananthasuresh, G. K., and Misra, S., 2021, "Surgical Applications of Compliant Mechanisms: A Review," ASME J. Mech. Rob., **13**(2), p. 020801.
[28] Xiao, Q., Musa, M., Godage, I. S., Su, H., and Chen, Y., 2023, "Kinematics and Stiffness Modeling of Soft Robot With a Concentric Backbone," ASME J. Mech. Rob., **15**(5), p. 051011.
[29] Granna, J., Godage, I. S., Wirz, R., Weaver, K. D., Webster, R. J., and Burgner-Kahrs, J., 2016, "A 3-D Volume Coverage Path Planning Algorithm With Application to Intracerebral Hemorrhage Evacuation," IEEE Robot. Autom. Lett., **1**(2), pp. 876–883.
[30] Gilbert, H. B., Neimat, J., and Webster, R. J., 2015, "Concentric Tube Robots as Steerable Needles: Achieving Follow-the-Leader Deployment," IEEE Trans. Rob., **31**(2), pp. 246–258.
[31] Sears, P., and Dupont, P., 2006, "A Steerable Needle Technology Using Curved Concentric Tubes," Proceedings of the 2006 IEEE/RSJ International Conference on Intelligent Robots and Systems, Beijing, China, Oct. 9–15, IEEE, pp. 2850–2856.
[32] Burgner, J., Swaney, P. J., Lathrop, R. A., Weaver, K. D., and Webster, R. J., 2013, "Debulking From Within: A Robotic Steerable Cannula for Intracerebral Hemorrhage Evacuation," IEEE Trans. Biomed. Eng., **60**(9), pp. 2567–2575.
[33] Doody, M. M., Lonstein, J. E., Stovall, M., Hacker, D. G., Luckyanov, N., Land, C. E., and Collaborators, U. S. C. S., 2000, "Breast Cancer Mortality After Diagnostic Radiography: Findings From the US Scoliosis Cohort Study," Spine, **25**(16), pp. 2052–2063.
[34] Godage, I. S., Remirez, A. A., Wirz, R., Weaver, K. D., Burgner-Kahrs, J., and Webster, R. J., 2015, "Robotic Intracerebral Hemorrhage Evacuation: An in-Scanner Approach With Concentric Tube Robots," Proceedings of the 2015 IEEE/RSJ International Conference on Intelligent Robots and Systems (IROS), Hamburg, Germany, Sept. 28–Oct. 3, IEEE, pp. 1447–1452.
[35] Masamune, K., Kobayashi, E., Masutani, Y., Suzuki, M., Dohi, T., Iseki, H., and Takakura, K., 1995, "Development of an MRI-Compatible Needle Insertion Manipulator for Stereotactic Neurosurgery," J. Image Guid. Surg., **1**(4), pp. 242–248.
[36] Pandya, S., Motkoski, J. W., Serrano-Almeida, C., Greer, A. D., Latour, I., and Sutherland, G. R., 2009, "Advancing Neurosurgery With Image-Guided Robotics," J. Neurosurg., **111**(6), pp. 1141–1149.
[37] Sheng, J., and Desai, J. P., 2015, "Towards a SMA-Actuated Neurosurgical Intracerebral Hemorrhage Evacuation (NICHE) Robot," Proceedings of the 2015 IEEE/RSJ International Conference on Intelligent Robots and Systems (IROS), Hamburg, Germany, Sept. 28–Oct. 3, IEEE, pp. 3805–3810.
[38] Su, H., Li, G., Rucker, D. C., Webster, R. J. III, and Fischer, G. S., 2016, "A Concentric Tube Continuum Robot With Piezoelectric Actuation for MRI-Guided Closed-Loop Targeting," Ann. Biomed. Eng., **44**(10), pp. 2863–2873.
[39] Chen, Y., Godage, I. S., Sengupta, S., Liu, C. L., Weaver, K. D., and Barth, E. J., 2019, "MR-Conditional Steerable Needle Robot for Intracerebral Hemorrhage Removal," Int. J. Comput. Assist. Radiol. Surg., **14**(1), pp. 105–115.
[40] Gunderman, A. L., Sengupta, S., Siampli, E., Sigounas, D. G., Kellner, C. P., Oluigbo, C. O., Sharma, K., Godage, I., Cleary, K. R., and Chen, Y., 2023, "Non-Metallic MR-Guided Concentric Tube Robot for Intracerebral Hemorrhage Evacuation," IEEE Trans. Biomed. Eng.
[41] Shamir, R. R., Tamir, I., Dabool, E., Joskowicz, L., and Shoshan, Y., 2010, "A Method for Planning Safe Trajectories in Image-Guided Keyhole Neurosurgery," Proceedings of the Medical Image Computing and Computer-Assisted Intervention–MICCAI 2010: 13th International Conference, Part III 13, Beijing, China, Sept. 20–24, Springer, pp. 457–464.
[42] Shamir, R. R., Joskowicz, L., Tamir, I., Dabool, E., Pertman, L., Ben-Ami, A., and Shoshan, Y., 2012, "Reduced Risk Trajectory Planning in Image-Guided Keyhole Neurosurgery," Med. Phys., **39**(5), pp. 2885–2895.
[43] Flaßkamp, K., Worthmann, K., Mühlenhoff, J., Greiner-Petter, C., Büskens, C., Oertel, J., Keiner, D., and Sattel, T., 2019, "Towards Optimal Control of Concentric Tube Robots in Stereotactic Neurosurgery," Math. Comput. Modell. Dyn. Syst., **25**(6), pp. 560–574.
[44] Kunz, C., Gerst, M., Henrich, P., Schneider, M., Hlavac, M., Pala, A., and Mathis-Ullrich, F., 2021, "Multimodal Risk-Based Path Planning for Neurosurgical Interventions," ASME J. Med. Devices, **15**(1), p. 011108.
[45] Peikert, S., Kunz, C., Fischer, N., Hlaváč, M., Pala, A., Schneider, M., and Mathis-Ullrich, F., 2022, "Automated Linear and Non-Linear Path Planning for Neurosurgical Interventions," Proceedings of the 2022 International Conference on Robotics and Automation (ICRA), Philadelphia, PA, May 23–27, IEEE, pp. 7731–7737.
[46] Beaulieu, C., 2002, "The Basis of Anisotropic Water Diffusion in the Nervous System—A Technical Review," NMR Biomed., **15**(7–8), pp. 435–455.
[47] Hess, C. P., and Mukherjee, P., 2007, "Visualizing White Matter Pathways in the Living Human Brain: Diffusion Tensor Imaging and Beyond," Neuroimaging Clin. N. Am., **17**(4), pp. 407–426.
[48] Zhang, N., Zhang, F., Deng, Z., Yang, Q., Diniz, M. A., Song, S. S., Schlick, K. H., Marcel Maya, M., Gonzalez, N., and Li, D., 2018, "3D Whole-Brain Vessel Wall Cardiovascular Magnetic Resonance Imaging: A Study on the Reliability in the Quantification of Intracranial Vessel Dimensions," J. Cardiovasc. Magn. Reson., **20**(1), pp. 1–12.
[49] Yang, Q., Deng, Z., Bi, X., Song, S. S., Schlick, K. H., Gonzalez, N. R., Li, D., and Fan, Z., 2017, "Whole-Brain Vessel Wall MRI: A Parameter Tune-up Solution to Improve the Scan Efficiency of Three-Dimensional Variable Flip-Angle Turbo Spin-Echo," J. Magn. Reson. Imaging, **46**(3), pp. 751–757.
[50] Katoch, S., Chauhan, S. S., and Kumar, V., 2021, "A Review on Genetic Algorithm: Past, Present, and Future," Multimed. Tools Appl., **80**(5), pp. 8091–8126.
[51] Toponogov, V. A., 2006, "Differential Geometry of Curves and Surfaces: A Concise Guide," *Differential Geometry of Curves and Surfaces: A Concise Guide*, V. Y. Rovenski, ed., Boston, MA, pp. 1–206.
[52] Corbetta, M., Ramsey, L., Callejas, A., Baldassarre, A., Hacker, C. D., Siegel, J. S., Astafiev, S. V., et al., 2015, "Common Behavioral Clusters and Subcortical Anatomy in Stroke," Neuron, **85**(5), pp. 927–941.
[53] Labib, M. A., Shah, M., Kassam, A. B., Young, R., Zucker, L., Maioriello, A., Britz, G., Agbi, C., Day, J., and Gallia, G., 2017, "The Safety and Feasibility of Image-Guided Brainpath-Mediated Transsulcul Hematoma Evacuation: A Multicenter Study," Neurosurgery, **80**(4), pp. 515–524.
[54] Panesar, S. S., Abhinav, K., Yeh, F.-C., Jacquesson, T., Collins, M., and Fernandez-Miranda, J., 2019, "Tractography for Surgical Neuro-Oncology Planning: Towards a Gold Standard," Neurotherapeutics, **16**(1), pp. 36–51.
[55] Yeh, F. C., Panesar, S., Fernandes, D., Meola, A., Yoshino, M., Fernandez-Miranda, J. C., Vettel, J. M., and Verstynen, T., 2018, "Population-Averaged Atlas of the Macroscale Human Structural Connectome and Its Network Topology," Neuroimage, **178**(1), pp. 57–68.
[56] Mouches, P., and Forkert, N. D., 2019, "A Statistical Atlas of Cerebral Arteries Generated Using Multi-Center MRA Datasets From Healthy Subjects," Sci. Data, **6**(1), p. 29.
[57] Ray, N., Saha, B. N., and Brown, M. R. G., 2007, "Locating Brain Tumors From MR Imagery Using Symmetry," Proceedings of the 2007 Conference Record of the Forty-First Asilomar Conference on Signals, Systems and Computers, Pacific Grove, CA., Nov. 4–7, IEEE, pp. 224–228.
[58] Shen, J., Wang, Y., Azizkhani, M., Qiu, D., and Chen, Y., 2023, "Concentric Tube Robot Redundancy Resolution via Velocity/Compliance Manipulability Optimization," IEEE Robot. Autom. Lett., **8**(11), pp. 7495–7502.